Article:

Xu, H. orcid.org/0009-0004-5156-4460, Zhu, Z.Q. orcid.org/0000-0001-7175-3307, Yang, L. et al. (2 more authors) (2025) Decomposition and investigation of torque components of dual-PM machines. IET Electric Power Applications, 19 (1). e70024. ISSN 1751-8660

https://doi.org/10.1049/elp2.70024

IET Electric Power Applications

WILEY

The Institution of Engineering and Technology

ORIGINAL RESEARCH OPEN ACCESS

Decomposition and Investigation of Torque Components of Dual-PM Machines

Hai Xu[1] | Zi Qiang Zhu[1] | Lei Yang[2] | Liang Chen[2] | Yanjian Zhou[2]

[1]Department of Electronic and Electrical Engineering, University of Sheffield, Sheffield, UK | [2]Corporate Research Center of Midea Group, Fu Shan, China

Correspondence: Zi Qiang Zhu (z.q.zhu@sheffield.ac.uk)

Received: 11 December 2024 | **Revised:** 17 February 2025 | **Accepted:** 14 March 2025

Handling Editor: David Gerada

Funding: This work is supported by the Midea Group, P. R. China under R/174939-11-1.

Keywords: dual permanent magnet | permanent magnet machine | torque components | torque decomposition | vernier machines

ABSTRACT

This paper proposes a multi-torque component decomposition method combining with frozen permeability method, and for the first time, accurately decomposes six torque components of dual-PM (DPM) machines. Based on the decomposition results, the characteristics of torque components are investigated. It is found that for average torque, the components generated by armature field interacting with PM fields and iron cores have positive contributions, while the components generated by the interactions between stator PMs, rotor PMs, and iron cores have negative contributions and are affected by magnetic saturation. The phases of torque ripple of torque components are different, resulting in a low resultant torque ripple of DPM machines. Moreover, for cogging torque, the component generated by the interaction between stator PMs and rotor PMs is the major source, and the components generated by the interactions between PMs and iron poles have a cancelling effect. Finally, a DPM machine is prototyped and tested to verify the analyses.

1 | Introduction

As the requirements for machine torque density become higher and higher, field modulated and magnetically geared permanent magnet (PM) machines have gained increasing attention [1]. Based on the position of PMs, the field modulated and magnetically geared PM machines are usually classified into two categories, that is, stator-PM machines [2–4] and rotor-PM machines [5–7]. To achieve further torque improvement, dual-PM (DPM) machines combining stator-PM machines and rotor-PM machines are proposed and investigated [8]. In DPM machines, the PMs are located in both salient stator and rotor, so that the field modulation effect and magnetic gearing effect can be achieved from both stator and rotor sides.

In 1995, a DPM machine was proposed for the first time in ref. [8]. The stator used open slots with tooth tips and overlapping distributed windings, and PMs were put in slot openings. The rotor was a consequent-pole structure. Based on this typical topology, many novel DPM machines were proposed to achieve further torque improvement. For the stator side, the multi-tooth configuration with non-overlapping concentrated windings was used to reduce the length of end windings and increase the gear ratio by increasing the pole numbers of stator and rotor [9–12]. Spoke-type [13, 14] and Halbach [15] PM arrangements were used to enhance the stator PM field, and DC field windings were used to realise hybrid excitation and improve the flux weakening performance [16, 17]. For the rotor side, V-type [18], spoke-type [13], and Halbach [9, 19] consequent-pole PM arrangements were used to enhance the rotor PM field. In ref.

[20], DPM machines with another set of armature windings in the rotor were proposed to improve torque density and fault tolerant capability.

In addition to topological innovations, the field modulation and magnetic gearing effects and the torque production mechanism of DPM machines were also investigated in refs. [21–25]. The torques generated by stator PMs and rotor PMs were quantified in refs. [23, 24]. In ref. [25], the significance of torque contributions of stator PMs and rotor PMs were investigated and found to be determined by the relationship between stator and rotor pole numbers. In most existing literature, the torque components of DPM machines are typically considered to consist of only two components generated by the armature field interacting with the stator and rotor PMs. The field modulation and magnetic gearing effects, as commonly used analytical techniques for analysing the torque generation mechanism of field modulated and magnetically geared PM machines, can only analyse these two components. However, compared with the single-PM machines, DPM machines have very complicated torque components due to multiple magnetic field excitations. For example, the torque component generated by the attraction and repulsion between the stator PMs and the rotor PMs only exists in DPM machines, which has not been reported and investigated. The torque components of DPM machines have not been identified, and the method to accurately decompose the torque components is still absent. This may result in low accuracy for investigating torque characteristics of DPM machines.

On the other hand, since the frozen permeability method is able to consider the magnetic saturation effect, it is applied to decompose torque components of various types of PM machines [26, 27].

Therefore, this paper proposes a multi-torque component decomposition (MTCD) method combining with frozen permeability method. The frozen permeability method is incorporated into the proposed method to consider the magnetic saturation effect and improve the accuracy. This paper, for the first time, accurately decomposes six torque components of DPM machines and reveal the torque production mechanism from the perspective of interaction between magnetic fields and iron cores. Moreover, the characteristics of torque components under different conditions are analysed after decomposing the torque components by the proposed method. It is found that the components generated by armature field interacting with PM fields and iron cores contribute positively to average torque, whereas the components generated by the interactions between stator PMs, rotor PMs, and iron cores contribute negatively to average torque and are affected by magnetic saturation. The torque ripple phases of various torque components are different, resulting in a low resultant torque ripple of DPM machines. The component generated by the interaction between stator PMs and rotor PMs is the major source of the cogging torque, and the components generated by the interactions between PMs and iron poles tend to counteract the cogging torque.

This paper is organised as follows. In Section 2, the machine topology and operation principle of DPM machines are introduced. In Section 3, the torque components generated by interactions of different magnetic fields and iron cores are illustrated and the MTCD method combining with frozen permeability method is introduced. In Section 4, the characteristics of torque components in cogging torque and on-load torque with different armature currents are investigated. In Section 5, a DPM machine is prototyped and tested to validate the analyses. Finally, the conclusions are presented in Section 6.

2 | Machine Topology and Operation Principle

Figure 1 shows a DPM machine having 12 pole-pair-stator and 10 pole-pair-rotor to demonstrate the typical machine topology. For stator side, the PMs are put in slot openings. For rotor side, the PMs are placed between the iron poles, forming a consequent-pole rotor. The PMs are all magnetised in the radial direction. All PMs have the same polarity to achieve high torque density. The iron poles in stator and rotor are modulators which modulate the rotor PM field and stator PM field, respectively.

The DPM machines operate based on field modulation effect and magnetic gearing effect from both stator and rotor sides. The operation principle can be descripted as follows.

The flux leakage, fringing effect, and magnetic saturation of stator and rotor iron cores are all ignored for simplicity. The magnetomotive forces (MMFs) of stator PMs and rotor PMs are defined as follows:

$$F_{\mathrm{SPM}}(\theta) = \sum_{i=1}^{\infty} F_{\mathrm{SPM}i} \cos(ip_{\mathrm{S}}\theta) \tag{1}$$

$$F_{\mathrm{RPM}}(\theta, t) = \sum_{k=1}^{\infty} F_{\mathrm{RPM}k} \cos[kp_{\mathrm{R}}(\theta - \omega_{\mathrm{R}}t)] \tag{2}$$

The airgap permeances of slotted stator and rotor are

$$P_{\mathrm{S}}(\theta) = \sum_{j=0}^{\infty} P_{\mathrm{S}j} \cos(jp_{\mathrm{S}}\theta + \pi) \tag{3}$$

$$P_{\mathrm{R}}(\theta, t) = \sum_{m=0}^{\infty} P_{\mathrm{R}m} \cos[mp_{\mathrm{R}}(\theta - \omega_{\mathrm{R}}t) + \pi] \tag{4}$$

where ω_{R} is the mechanical angular velocity of rotor, p_{S} and p_{R} are the pole-pair numbers of stator and rotor PMs, and $F_{\mathrm{SPM}i}$,

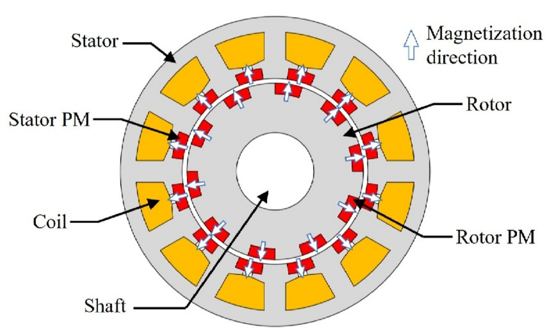

FIGURE 1 | Demonstration of DPM machines.

F_{RPMk}, P_{Sj} and P_{Rm} are the amplitudes of PM MMFs and airgap permeances of stator and rotor, respectively. The integers, i, j, k and m, represent the orders of harmonics.

The stator PM field and rotor PM field are modulated by rotor iron poles and stator iron poles, respectively. According to the MMF-permeance model, the open-circuit airgap flux density is the product of PM MMF and airgap permeance and can be obtained as follows:

$$
\begin{aligned}
&B_{PM}(\theta, t) = F_{SPM}(\theta)P_R(\theta, t) + F_{RPM}(\theta, t)P_S(\theta) \\
&= \frac{1}{2}\sum_{i=1}^{\infty}\sum_{m=0}^{\infty} F_{SPMi}P_{Rm}\cos(ip_S \pm mp_R)\left(\theta \mp \frac{mp_R\omega_R t}{ip_S \pm mp_R}\right) \\
&+ \frac{1}{2}\sum_{k=1}^{\infty}\sum_{j=0}^{\infty} F_{RPMk}P_{Sj}\cos(kp_R \pm jp_S)\left(\theta - \frac{kp_R\omega_R t}{kp_R \pm jp_S}\right)
\end{aligned}
\tag{5}
$$

The armature windings are fed by 3-phase sinusoidal currents which can be expressed as follows:

$$
\begin{cases}
i_a(t) = I_{ph}\sin(p_a\omega_a t) \\
i_b(t) = I_{ph}\sin(p_a\omega_a t - 2\pi/3) \\
i_c(t) = I_{ph}\sin(p_a\omega_a t - 4\pi/3)
\end{cases}
\tag{6}
$$

where I_{ph} is the amplitude of phase current, ω_a is the mechanical angular velocity of armature field, and p_a is the armature pole-pair number.

Hence, the armature MMF is

$$
\begin{cases}
F_a(\theta, t) = \sum_{v}^{\infty} F_{Av}\sin(vp_a\theta \pm p_a\omega_a t) \\
F_{Av} = \dfrac{3N_{ph}I_{ph}k_{wvp_a}}{\pi v p_a} \\
v = |6n \pm 1|, n = 0, 1, 2, \ldots
\end{cases}
\tag{7}
$$

where N_{ph} is the number of turns per phase, v and n are the integer numbers, and k_{wvp_a} is the winding factor of vp_a pole-pair harmonics.

Similar to the PM field, the airgap flux density produced by armature MMF can also be obtained by the MMF-permeance model as follows:

$$
B_a(\theta, t) = F_a(\theta, t)P_{airgap}(\theta, t) \tag{8}
$$

In DPM machines, the stator and rotor are slotted and the slot openings cannot be neglected, and thus, they are doubly salient structure. The armature MMF is modulated by both stator and rotor iron poles. The airgap permeance considering slot effect of both stator and rotor is [21]

$$
P_{airgap}(\theta, t) \approx P_S(\theta)P_R(\theta, t)\mu_0/g \tag{9}
$$

Hence, the airgap flux density produced by armature MMF is defined as follows:

$$
\begin{aligned}
&B_a(\theta, t) = F_a(\theta, t)P_S(\theta)P_R(\theta, t)\mu_0/g \\
&= \frac{\mu_0}{4g}\sum_{v}^{\infty}\sum_{j=0}^{\infty}\sum_{m=0}^{\infty} F_{Av}P_{Sj}P_{Rm}\sin\Big[(vp_a \pm jp_S \pm mp_R) \\
&\left(\theta \pm \frac{p_a\omega_a \pm mp_R\omega_R}{vp_a \pm jp_S \pm mp_R}t\right)\Big]
\end{aligned}
\tag{10}
$$

The harmonic characteristics of PM field and armature field are summarised in Table 1.

To generate average torque, the armature field and PM field should have the same pole-pair number and mechanical angular velocity. Hence, for DPM machines, the following equations should be satisfied:

$$
\begin{cases}
ip_S \pm m_1p_R = vp_a \pm jp_S \pm m_2p_R \\
\dfrac{m_1p_R\omega_R}{ip_S \pm m_1p_R} = \dfrac{p_a\omega_a \pm m_2p_R\omega_R}{vp_a \pm jp_S \pm m_2p_R} \\
v = |6n \pm 1|, n = 0, 1, 2, \ldots \\
i, j, m_1, m_2 = 0, 1, 2, \ldots
\end{cases}
$$

$$
\begin{cases}
kp_R \pm j_1p_S = vp_a \pm j_2p_S \pm mp_R \\
\dfrac{kp_R\omega_R}{kp_R \pm j_1p_S} = \dfrac{p_a\omega_a \pm mp_R\omega_R}{vp_a \pm j_2p_S \pm mp_R} \\
v = |6n \pm 1|, n = 0, 1, 2, \ldots \\
k, j_1, j_2, m = 0, 1, 2, \ldots
\end{cases}
\tag{11}
$$

In DPM machines, the stator PM field and rotor PM field are modulated by rotor iron poles and stator iron poles, respectively, and the armature field is modulated by both stator and rotor iron poles. This is the production mechanism of the torque components generated by the armature field interacting with the stator and rotor PMs from the perspective of field modulation effect. Other torque components of DPM machines are difficult to quantify by analytical techniques.

In this paper, by way of example, the investigations are carried out on a 12 pole-pair-stator and 10 pole-pair-rotor DPM machine. The 3-phase currents under zero d-axis ($i_d = 0$) current control are applied in the 2-pole-pair armature windings. The cross section and open-circuit field distribution are shown in Figure 2, and the parameters are listed in Table 2.

TABLE 1 | Harmonic characteristics of PM and armature fields.

	Pole pairs	Mechanical angular velocity
PM field	$ip_S \pm mp_R$	$\frac{mp_R\omega_R}{ip_S \pm mp_R}$
	$kp_R \pm jp_S$	$\frac{kp_R\omega_R}{kp_R \pm jp_S}$
Armature field	$vp_a \pm jp_S \pm mp_R$	$\frac{p_a\omega_a \pm mp_R\omega_R}{vp_a \pm jp_S \pm mp_R}$

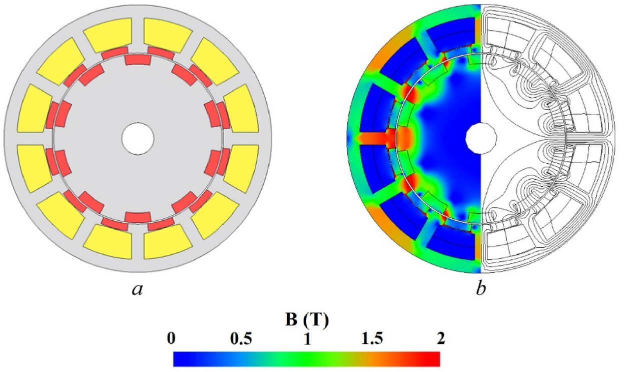

FIGURE 2 | Investigated DPM machine. (a) Topology. (b) Open-circuit field distribution.

TABLE 2 | Parameters of DPM machine.

Parameter	Value
Number of rotor pole pairs	10
Number of stator pole pairs	12
Number of armature pole pairs	2
Turns per phase	192
PM remanence (T)	1.2
Slot fill factor	0.5
Rotating speed (r/min)	240
Rated current (A)	8.2
Rated torque (Nm)	14.7
Airgap length (mm)	0.5
Lamination length (mm)	50
Stator outer diameter (mm)	100
Stator inner diameter (mm)	64
Yoke thickness (mm)	4.8
Tooth width (mm)	4.7
Slot opening (mm)	2.7
Tooth tip thickness (mm)	0.7
Stator PM thickness (mm)	2.7
Stator PM pole arc (deg.)	17.1
Rotor PM thickness (mm)	3.7
Rotor PM pole arc (deg.)	18.4

3 | Torque Component Decomposition

In DPM machines, there are three magnetic field excitations (stator PMs, rotor PMs and armature windings) and two iron cores (stator and rotor). All these magnetic fields and iron cores may interact with each other to generate torque. Hence, the torque components of DPM machines are more complicated than those of single-PM machines. The interactions of different magnetic fields and iron cores can be illustrated in Figure 3, and the resulting torque components are listed in Table 3.

Hence, accounting for all the interactions of different magnetic fields and iron cores, the torque of DPM machines consists of 6 components, and can be expressed as follows:

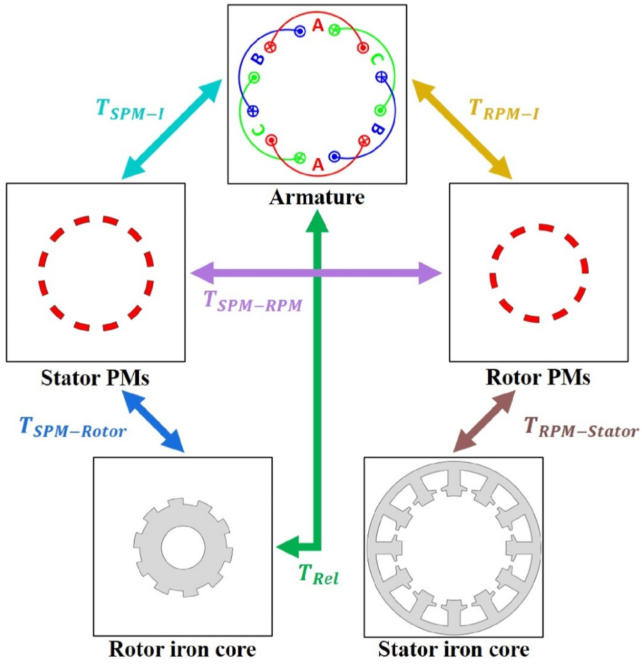

FIGURE 3 | Illustration of interactions of different magnetic fields and iron cores.

TABLE 3 | Torque components of DPM machines.

	Description
$T_{\mathrm{SPM}-I}$	Stator PM field interacts with armature field
$T_{\mathrm{RPM}-I}$	Rotor PM field interacts with armature field
$T_{\mathrm{SPM-RPM}}$	Stator PM field interacts with rotor PM field
$T_{\mathrm{SPM-Rotor}}$	Stator PM field interacts with rotor iron core
$T_{\mathrm{RPM-Stator}}$	Rotor PM field interacts with stator iron core
T_{Rel}	Armature field interacts with rotor iron core

$$T_{\mathrm{DPM}} = T_{\mathrm{SPM}-I} + T_{\mathrm{RPM}-I} + T_{\mathrm{SPM-RPM}} + T_{\mathrm{SPM-Rotor}} + T_{\mathrm{RPM-Stator}} + T_{\mathrm{Rel}} \tag{12}$$

The torque components $T_{\mathrm{SPM}-I}$ and $T_{\mathrm{RPM}-I}$ are generated by the armature field interacting with the stator PM field and the rotor PM field based on the field modulation and magnetic gearing effects, respectively.

The torque components $T_{\mathrm{SPM-Rotor}}$ and $T_{\mathrm{RPM-Stator}}$ can be considered as the cogging torques generated by the attractive force between the stator PMs and the rotor iron poles, and the attractive force between the rotor PMs and the stator teeth, respectively. Similarly, the torque component $T_{\mathrm{SPM-RPM}}$ can be considered to be generated by the attractive force between the stator PMs and the rotor PMs.

It should be noted that the torque component generated by the armature field interacting with the rotor iron core is the reluctance torque, and thus, represented by T_{Rel}. Although the average value of reluctance torque may be trivial since DPM machines usually operate under zero d-axis ($i_d = 0$) current control, the instantaneous value of the reluctance torque has a non-negligible effect on the actual torque ripple.

3.1 | Without Using Frozen Permeability Method

Based on above analyses, a MTCD method using finite element analysis (FEA) is proposed to separate all torque components of DPM machines. Figure 4 shows the flow chart of the MTCD method. Firstly, the MTCD method without using frozen permeability method is investigated, that is, the part without the red lines in Figure 4. Each step can be introduced in detail as follows.

Step 1: The on-load FEA of the DPM machine is performed to obtain the actual torque of the DPM machine.

$$T_1 = T_{\mathrm{DPM}} \tag{13}$$

Step 2: The rotor PMs are removed, and the on-load FEA of the resulting stator-PM machine is performed. The obtained torque contains three components generated by the interactions of armature field, stator PM field, and rotor iron core.

$$T_2 = T_{\mathrm{SPM}-I} + T_{\mathrm{SPM-Rotor}} + T_{\mathrm{Rel}} \tag{14}$$

Step 3: The stator PMs are removed, and the on-load FEA of the resulting rotor-PM machine is performed. The obtained torque contains three components generated by the interactions of armature field, rotor PM field, and stator and rotor iron cores.

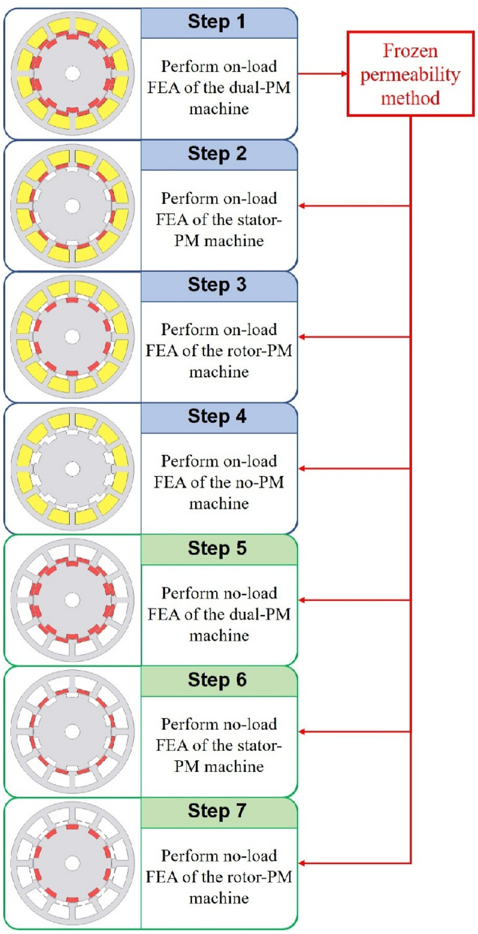

FIGURE 4 | Flow chart of MTCD method with/without using frozen permeability method.

$$T_3 = T_{\mathrm{RPM}-I} + T_{\mathrm{RPM-Stator}} + T_{\mathrm{Rel}} \tag{15}$$

Step 4: The stator and rotor PMs are removed, and the on-load FEA of the resulting no-PM machine is performed. The obtained torque contains one component generated by the interactions of armature field and rotor iron core.

$$T_4 = T_{\mathrm{Rel}} \tag{16}$$

Step 5: The no-load FEA of the DPM machine is performed. The obtained torque contains three components generated by the interactions of stator PM field, rotor PM field, and stator and rotor iron cores.

$$T_5 = T_{\mathrm{SPM-RPM}} + T_{\mathrm{SPM-Rotor}} + T_{\mathrm{RPM-Stator}} \tag{17}$$

Step 6: The rotor PMs are removed, and the no-load FEA of the resulting stator-PM machine is performed. The obtained torque contains one component generated by the interactions of stator PM field and rotor iron core.

$$T_6 = T_{\mathrm{SPM-Rotor}} \tag{18}$$

Step 7: The stator PMs are removed, and the no-load FEA of the resulting rotor-PM machine is performed. The obtained torque contains one component generated by the interactions of rotor PM field and stator iron core.

$$T_7 = T_{\mathrm{RPM-Stator}} \tag{19}$$

According to Equations (13)–(19), the torque components can be calculated by the following:

$$\begin{cases} T_{\mathrm{DPM}} = T_1 \\ T_{\mathrm{SPM}-I} = T_2 - T_4 - T_6 \\ T_{\mathrm{RPM}-I} = T_3 - T_4 - T_7 \\ T_{\mathrm{SPM-RPM}} = T_5 - T_6 - T_7 \\ T_{\mathrm{SPM-Rotor}} = T_6 \\ T_{\mathrm{RPM-Stator}} = T_7 \\ T_{\mathrm{Rel}} = T_4 \end{cases} \tag{20}$$

In order to verify the accuracy of the proposed MTCD method, the rated torque of the 12 pole-pair-stator and 10 pole-pair-rotor DPM machine is decomposed by this method. The waveforms of all torque components are plotted in Figure 5. The actual torque and the sum of all torque components are also included for comparison.

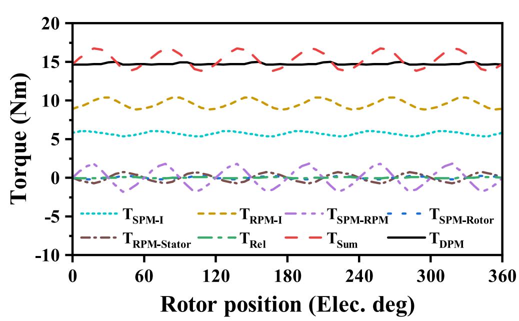

FIGURE 5 | Rated torque decomposition of DPM machine without frozen permeability method.

It can be seen that the sum of all torque components does not match the actual torque and exhibits significantly higher torque ripple. The reason is that the magnetic saturation conditions in Steps 1–7 are different, resulting in inaccurate average values and waveforms.

3.2 | Using Frozen Permeability Method

In order to obtain accurate torque components, the frozen permeability method [26, 27] is used to keep the magnetic saturation conditions of stator and rotor iron cores constant during the torque decomposition. The flow chart of MTCD method using frozen permeability method is also shown in Figure 4 (with red lines). In Step 1, the on-load FEA of the DPM machine is performed as the same as before. Then, the FEAs of Steps 2–7 are performed and the frozen permeability method is used to keep the magnetic saturation conditions consistent with Step 1.

The waveforms of all torque components and their sum and actual torque of the 12S10R DPM machine are plotted in Figure 6. It can be clearly seen that the waveforms of the sum of all torque components and the actual torque are almost the same. Hence, the proposed MTCD method combining frozen permeability method can accurately decompose all torque components of DPM machines.

It should be noted that the average values of torque components of $T_{SPM-RPM}$, $T_{SPM-Rotor}$, $T_{RPM-Stator}$ and T_{Rel} are not 0. The reason is that the distortion of permeability distribution in stator and rotor cores caused by the superposition of armature field, stator PM field, and rotor PM field is considered after using the frozen permeability method. The magnetic field distributions obtained by Steps 4–7 with and without using frozen permeability method are compared in Figure 7. The magnetic fields in the machines of Steps 4–7 without using frozen permeability method are symmetrically distributed. On the other hand, the magnetic field distributions become asymmetric after using frozen permeability method, since the armature field and PM fields make the permeability distribution in stator and rotor iron cores asymmetric. The distortion of permeability distribution can be considered as an equivalent magnetic saliency in stator and rotor iron cores. It should be noted that the armature field and PM fields are rotational, and thus, the equivalent magnetic saliency is also rotational. Consequently, the armature field and PM fields interact with the rotational equivalent magnetic saliency, and the non-zero torque components $T_{SPM-RPM}$, $T_{SPM-Rotor}$, $T_{RPM-Stator}$ and T_{Rel} are generated. In addition, it can be seen that the torque ripples of all torque components are also affected by the distortion of permeability distribution.

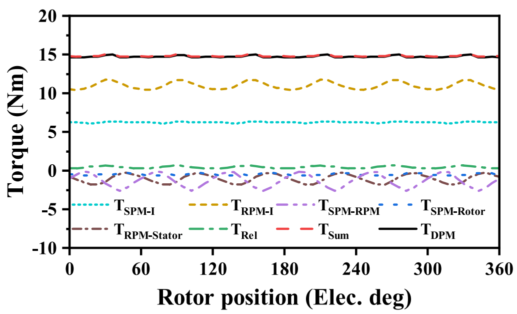

FIGURE 6 | Rated torque decomposition of DPM machine with frozen permeability method.

4 | Torque Characteristics

After accurately decomposing the torque components of DPM machines, the torque characteristics can be investigated.

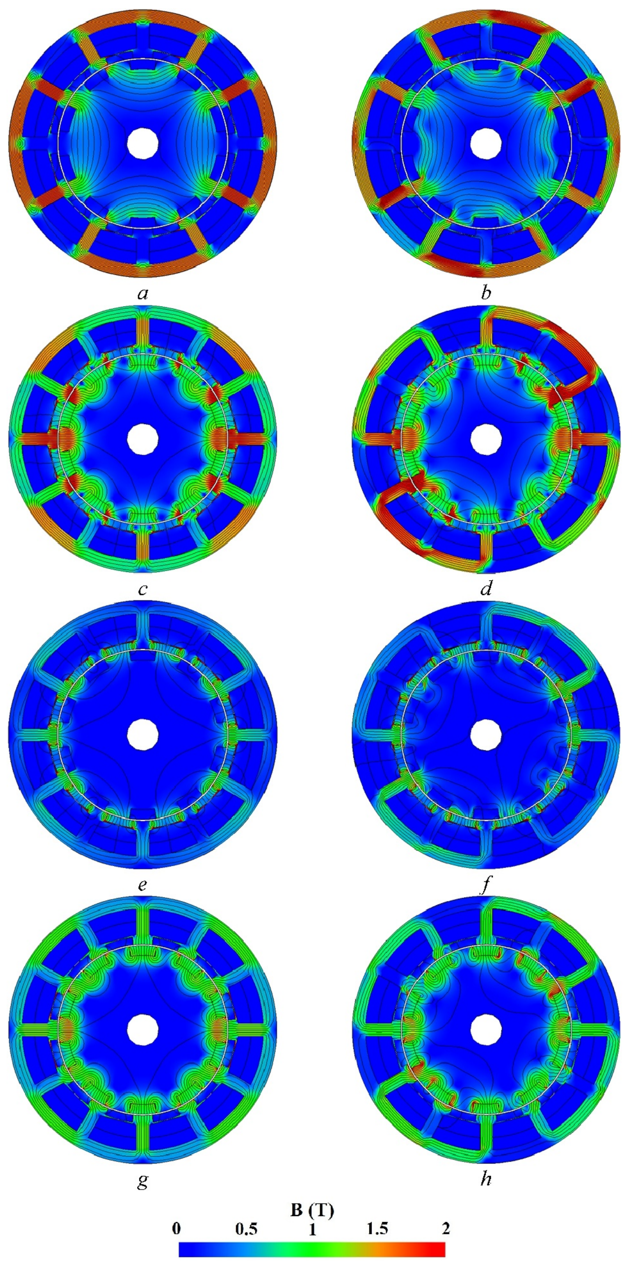

FIGURE 7 | Magnetic field distributions. (a) Step 4, (c) Step 5, (e) Step 6, (g) Step 7 without frozen permeability method. (b) Step 4, (d) Step 5, (f) Step 6, (h) Step 7 with frozen permeability method.

4.1 | Cogging Torque

The cogging torque is generated by the interactions between PMs and iron cores. Hence, the cogging torque contains three components and can be expressed as follows:

$$T_{\mathrm{Cogging}} = T_{\mathrm{SPM-RPM}} + T_{\mathrm{SPM-Rotor}} + T_{\mathrm{RPM-Stator}} \tag{21}$$

The flow chart of decomposing the torque components of cogging torque is shown in Figure 8. The cogging torque components T_{Cogging}, $T_{\mathrm{SPM-Rotor}}$ and $T_{\mathrm{RPM-Stator}}$ are obtained by Step 1, Step 2 and Step 3 in Figure 8, respectively. Hence, the component $T_{\mathrm{SPM-RPM}}$ can be obtained by the following:

$$T_{\mathrm{SPM-RPM}} = T_{\mathrm{Cogging}} - T_{\mathrm{SPM-Rotor}} - T_{\mathrm{RPM-Stator}} \tag{22}$$

The waveforms, spectra, and phases of cogging torque components of the DPM machine are shown in Figure 9.

The 6th order component is the main part of all cogging torque components. As can be seen, the 6th order components of $T_{\mathrm{SPM-Rotor}}$ and $T_{\mathrm{RPM-Stator}}$ have the same phase, while that of $T_{\mathrm{SPM-RPM}}$ has the opposite phase. The reason can be explained as follows. For the torque component generated by the interaction between the PMs and the iron poles ($T_{\mathrm{SPM-Rotor}}$ and $T_{\mathrm{RPM-Stator}}$), it is 0 when PMs are aligned with iron poles, and it is the peak when PMs are aligned with the air. For the torque component generated by the interaction between stator PMs and rotor PMs ($T_{\mathrm{SPM-RPM}}$), it is 0 when stator PMs and rotor PMs are aligned, and it is the peak when PMs are aligned with the air. In DPM machines, when stator PMs are aligned with rotor iron poles, rotor PMs are also aligned with stator iron poles, but stator PMs and rotor PMs are not aligned. At this moment, $T_{\mathrm{SPM-Rotor}}$ and $T_{\mathrm{RPM-Stator}}$ are 0, and $T_{\mathrm{SPM-RPM}}$ is the peak. When stator PMs and rotor PMs are aligned, stator PMs are not aligned with rotor iron poles, and rotor PMs are also not aligned with stator iron poles. At this moment, $T_{\mathrm{SPM-Rotor}}$ and $T_{\mathrm{RPM-Stator}}$ are the peak, and $T_{\mathrm{SPM-RPM}}$ is 0.

Owing to the opposite phase between $T_{\mathrm{SPM-Rotor}} + T_{\mathrm{RPM-Stator}}$ and $T_{\mathrm{SPM-RPM}}$, $T_{\mathrm{SPM-Rotor}}$ and $T_{\mathrm{RPM-Stator}}$ counteract a part of $T_{\mathrm{SPM-RPM}}$, and the peak value of T_{Cogging} is lower than that of $T_{\mathrm{SPM-RPM}}$, as illustrated in Figure 10. Hence, the component generated by the interaction between stator PMs and rotor PMs ($T_{\mathrm{SPM-RPM}}$) is the major source of the cogging torque, and the components generated by the interaction between the PMs and the iron poles ($T_{\mathrm{SPM-Rotor}}$ and $T_{\mathrm{RPM-Stator}}$) have a cancelling effect on the cogging torque.

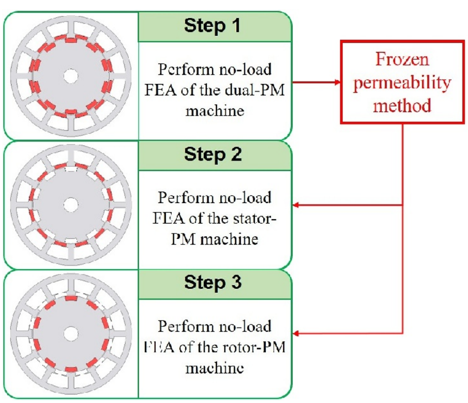

FIGURE 8 | Flow chart of decomposing cogging torque.

4.2 | Rated Torque

The torque components of the rated torque of the DPM machine are shown in Figure 6. The spectra and phases of torque components are shown in Figure 11. Figure 11a shows the amplitudes of different components, including average torque (0-order component) and torque ripple (6- and 12-order components), expressed in absolute values. Figure 11b shows the phases of different components. From Figure 11b, it can be seen that the phases of 0-order T_{DPM}, $T_{\mathrm{SPM}-I}$, $T_{\mathrm{RPM}-I}$ and T_{Rel} are 0° and those of 0-order $T_{\mathrm{SPM-Rotor}}$, $T_{\mathrm{RPM-Stator}}$ and $T_{\mathrm{SPM-RPM}}$ are 180°, which means the average torques of T_{DPM}, $T_{\mathrm{SPM}-I}$, $T_{\mathrm{RPM}-I}$

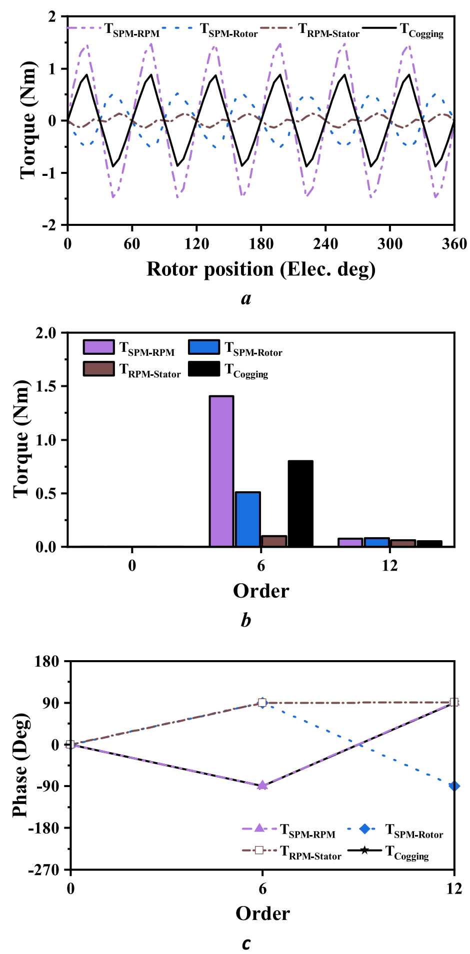

FIGURE 9 | Cogging torque decomposition of DPM machine. (a) Waveforms. (b) Spectra. (c) Phase.

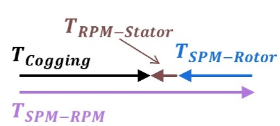

FIGURE 10 | Phasor diagram of 6th order cogging torque components of DPM machine.

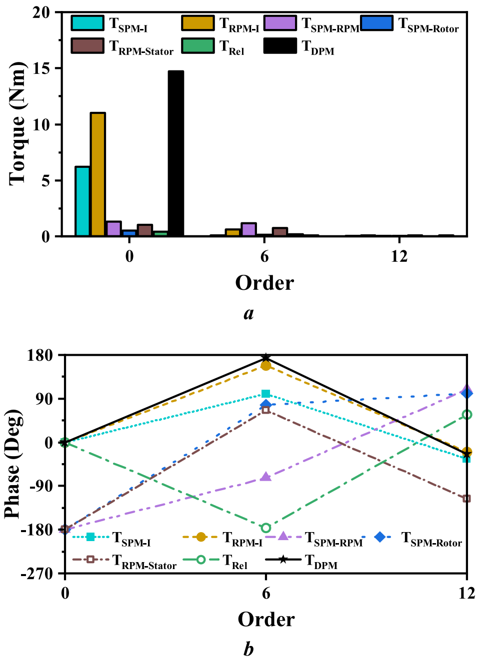

FIGURE 11 | Rated torque decomposition of DPM machine. (a) Spectra. (b) Phase.

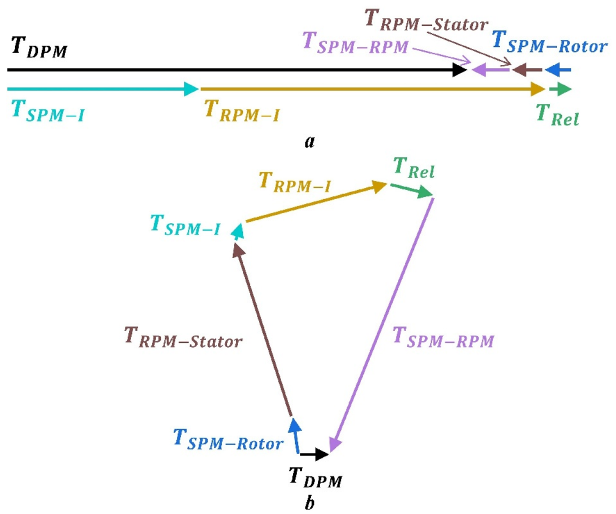

FIGURE 12 | Phasor diagrams of rated torque of DPM machine. (a) Average torque. (b) Sixth order component.

and T_{Rel} are positive and those of $T_{\text{SPM-Rotor}}$, $T_{\text{RPM-Stator}}$ and $T_{\text{SPM-RPM}}$ are negative. According to the spectra and phases, the phasor diagrams of average torque and the 6th order component can be plotted in Figure 12.

It can be seen that the torque components generated by the armature field interacting with the PM fields ($T_{\text{SPM}-I}$ and $T_{\text{RPM}-I}$) make the major contribution to average torque. The reluctance torque (T_{Rel}) contributes positively to average torque but the value is low. However, the torque components generated by the interactions between PMs and iron cores ($T_{\text{SPM-Rotor}}$, $T_{\text{RPM-Stator}}$ and $T_{\text{SPM-RPM}}$) have negative contributions to average torque.

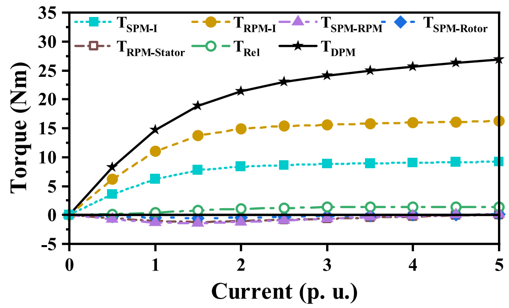

FIGURE 13 | Average torque components with different armature currents.

As for the torque ripple, the phases of the 6th order components of all torque components are different. Hence, although some torque components have relatively high ripples, the actual torque ripple of the DPM machine is low after the superposition of all components.

4.3 | Overload Capability

As discussed in Section 3, the torque components are affected by the distortion of permeability distribution which is determined by the magnetic saturation level. Hence, it is necessary to analyse the effect of armature reaction on the torque components. Figure 13 shows average values of all torque components with different armature currents.

The torque components generated by armature field interacting with PM fields and iron cores ($T_{\text{SPM}-I}$, $T_{\text{RPM}-I}$ and T_{Rel}) increase with the increase of armature current, but the increment diminishes quickly under overload condition. For these torque components, the magnetic saturation restricted the torque improvement.

On the other hand, for the torque components generated by the interactions between PMs and iron cores ($T_{\text{SPM-Rotor}}$, $T_{\text{RPM-Stator}}$ and $T_{\text{SPM-RPM}}$), the negative contributions increase first and then decrease with the increase of armature current. Although $T_{\text{SPM-Rotor}}$, $T_{\text{RPM-Stator}}$ and $T_{\text{SPM-RPM}}$ are not generated by armature field directly, these torque components are affected by armature currents due to the magnetic saturation in iron cores. When the magnetic saturation is severe, more severe magnetic saturation can reduce the negative contributions, which is beneficial to the torque improvement.

5 | Experimental Validation

A DPM machine is prototyped and tested to verify the FEA analyses. The specifications of the prototype are listed in Table 2. Figure 14 shows the photos of the DPM machine.

Figure 15 shows the FEA and test results of phase back-EMF of the DPM machine at 240 r/min. It can be seen that the test result of back-EMF is in a good agreement with the FEA result. The cogging torques are measured by using a simple cogging torque measurement method [28], as shown in

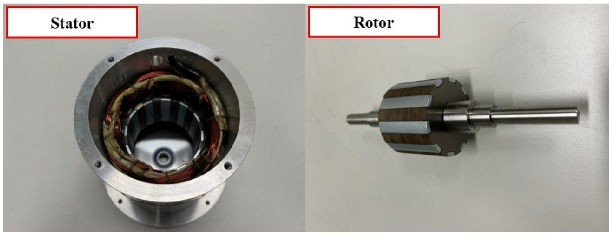

FIGURE 14 | Prototype.

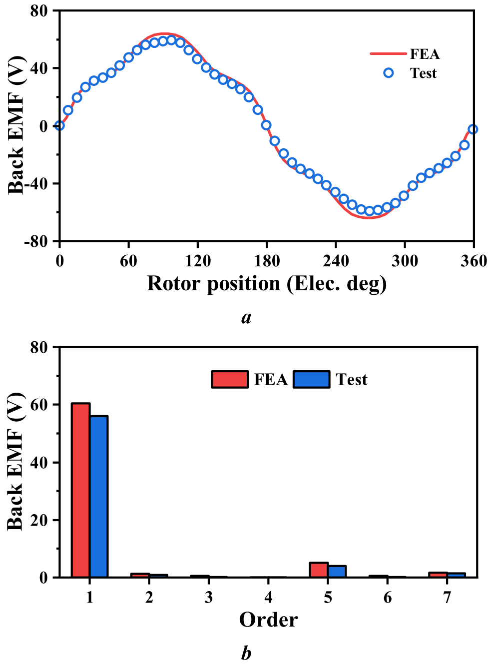

FIGURE 15 | Line back-EMF at 240 r/min. (a) Waveforms. (b) Spectra.

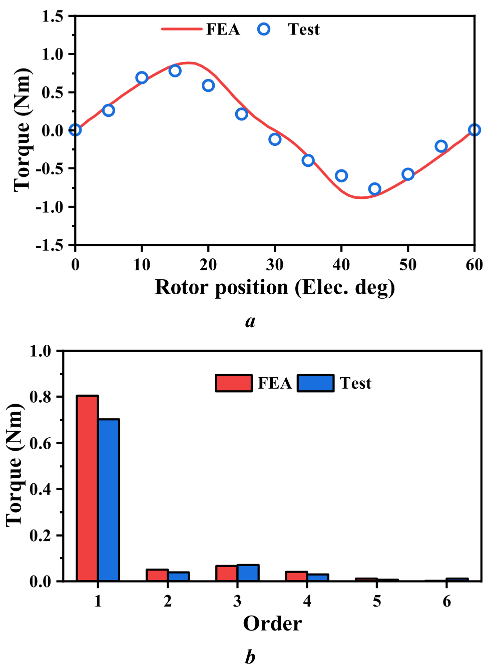

FIGURE 16 | Cogging torque. (a) Waveforms. (b) Spectra.

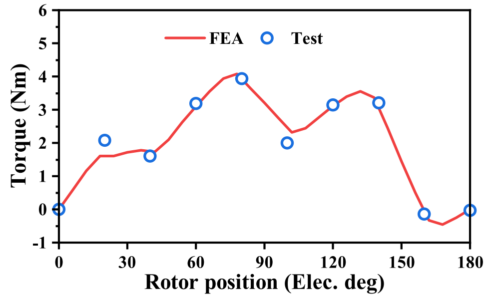

FIGURE 17 | Static torque ($I_a = -2I_b = -2I_c = 0.2I_{\text{rated}}$).

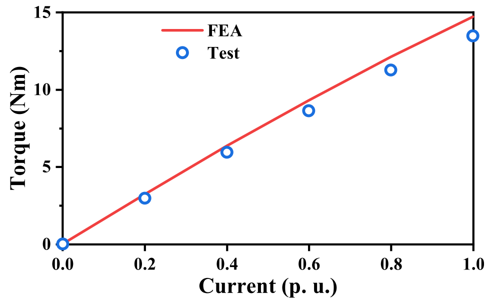

FIGURE 18 | Average torque with different currents.

Figure 16. Moreover, the static torque varying with rotor position can also be measured by applying DC current in the armature windings ($I_a = -2I_b = -2I_c = I_{\text{DC}}$ for a range of DC currents), as shown in Figure 17. The average torque with different currents is also measured and shown in Figure 18. It can be seen that the test results match well with the FEA results.

6 | Conclusion

This paper has proposed a technique for decomposing the torque components of DPM machines and investigated their characteristics. A MTCD method combining with the frozen permeability method is proposed. It is found that DPM machines have 6 torque components generated by different sources, and all torque components are accurately identified by the proposed method. Under on-load conditions, the components generated by armature field interacting with PM fields and iron cores ($T_{\text{SPM}-I}$, $T_{\text{RPM}-I}$ and T_{Rel}) contribute positively to average torque, while the components generated by the interactions between stator PMs, rotor PMs, and iron cores ($T_{\text{SPM}-\text{Rotor}}$, $T_{\text{RPM}-\text{Stator}}$ and $T_{\text{SPM}-\text{RPM}}$) contribute negatively to average torque and are affected by magnetic saturation. The phases of torque ripples of torque components are different, resulting in a low resultant torque ripple of DPM machines. Under the open-circuit condition, the component generated by the interaction between stator PMs and rotor PMs ($T_{\text{SPM}-\text{RPM}}$) is the major source of the cogging torque, and the components generated by the interaction between PMs and iron poles ($T_{\text{SPM}-\text{Rotor}}$ and $T_{\text{RPM}-\text{Stator}}$) have a cancelling effect on the cogging torque.

The proposed MTCD method combining frozen permeability method is applicable to DPM machines with any PM arrangements, and also can be extended to other machines containing multiple torque components.

Author Contributions

Hai Xu: investigation, methodology, writing – original draft. **Zi Qiang Zhu:** conceptualization, funding acquisition, project administration, resources, supervision, writing – review and editing. **Lei Yang:** funding acquisition, resources, supervision. **Liang Chen:** funding acquisition, resources, supervision. **Yanjian Zhou:** funding acquisition, resources, supervision.

Conflicts of Interest

The authors declare no conflicts of interest.

Data Availability Statement

Data available on request from the authors.

References

1. X. Zhu, C. H. T. Lee, C. C. Chan, L. Xu, and W. Zhao, "Overview of Flux-Modulation Machines Based on Flux-Modulation Principle: Topology, Theory, and Development Prospects," *IEEE Transactions on Transportation Electrification* 6, no. 2 (2020): 612–624, https://doi.org/10.1109/tte.2020.2981899.

2. I. Boldea, Z. Jichun, and S. A. Nasar, "Theoretical Characterization of Flux Reversal Machine in Low-Speed Servo Drives-the Pole-PM Configuration," *IEEE Transactions on Industry Applications* 38, no. 6 (2002): 1549–1557.

3. Y. Gao, R. Qu, D. Li, J. Li, and L. Wu, "Design of Three-Phase Flux-Reversal Machines With Fractional-Slot Windings," *IEEE Transactions on Industry Applications* 52, no. 4 (2016): 2856–2864, https://doi.org/10.1109/tia.2016.2535108.

4. Z. Z. Wu and Z. Q. Zhu, "Analysis of Air-Gap Field Modulation and Magnetic Gearing Effects in Switched Flux Permanent Magnet Machines," *IEEE Transactions on Magnetics* 51, no. 5 (2015): 1–12, https://doi.org/10.1109/tmag.2015.2402201.

5. J. Li, K. T. Chau, J. Z. Jiang, C. Liu, and W. Li, "A New Efficient Permanent-Magnet Vernier Machine for Wind Power Generation," *IEEE Transactions on Magnetics* 46, no. 6 (2010): 1475–1478, https://doi.org/10.1109/tmag.2010.2044636.

6. D. Li, R. Qu, and T. A. Lipo, "High-Power-Factor Vernier Permanent-Magnet Machines," *IEEE Transactions on Industry Applications* 50, no. 6 (2014): 3664–3674, https://doi.org/10.1109/tia.2014.2315443.

7. L. Fang, D. Li, X. Ren, and R. Qu, "A Novel Permanent Magnet Vernier Machine With Coding-Shaped Tooth," *IEEE Transactions on Industrial Electronics* 69, no. 6 (2022): 6058–6068, https://doi.org/10.1109/tie.2021.3088331.

8. A. Ishizaki, T. Tanaka, K. Takasaki, and S. Nishikata, "Theory and Optimum Design of PM Vernier Motor," in *1995 Seventh International Conference on Electrical Machines and Drives (Conf. Publ. No. 412)* (1995), 208–212.

9. D. K. Jang and J. H. Chang, "Design of a Vernier Machine With PM on Both Sides of Rotor and Stator," *IEEE Transactions on Magnetics* 50, no. 2 (2014): 877–880, https://doi.org/10.1109/tmag.2013.2284509.

10. S. Kazuhiro, R. Hosoya, and S. Shimomura, "Design of NdFeB Bond Magnets for In-Wheel Permanent Magnet Vernier Machine," in *2012 15th International Conference on Electrical Machines and Systems (ICEMS)* (2012), 1–6.

11. Q. Lin, S. Niu, F. Cai, W. Fu, and L. Shang, "Design and Optimization of a Novel Dual-PM Machine for Electric Vehicle Applications," *IEEE Transactions on Vehicular Technology* 69, no. 12 (2020): 14391–14400, https://doi.org/10.1109/tvt.2020.3034573.

12. H. Huang, D. Li, X. Ren, and R. Qu, "Analysis and Reduction Methods of Cogging Torque in Dual PM Vernier Machines With Unevenly Distributed Split Teeth," *IEEE Transactions on Industry Applications* 58, no. 4 (2022): 4637–4647, https://doi.org/10.1109/tia.2022.3173896.

13. Z. Liang, Y. Gao, D. Li, and R. Qu, "Design of a Novel Dual Flux Modulation Machine With Consequent-Pole Spoke-Array Permanent Magnets in Both Stator and Rotor," *CES Transactions on Electrical Machines and Systems* 2, no. 1 (2018): 73–81, https://doi.org/10.23919/tems.2018.8326453.

14. F. R. Wei, Z. Q. Zhu, and H. Qu, "Novel Dual-PM Spoke-Type Flux Reversal Machines," in *Proceedings of 16th International Conference on Ecological Vehicles and Renewable Energies (EVER)* (2021), 1–6.

15. K. Xie, D. Li, R. Qu, and Y. Gao, "A Novel Permanent Magnet Vernier Machine With Halbach Array Magnets in Stator Slot Opening," *IEEE Transactions on Magnetics* 53, no. 6 (2017): 1–5, https://doi.org/10.1109/tmag.2017.2658634.

16. Q. Wang and S. Niu, "A Novel Hybrid-Excited Dual-PM Machine With Bidirectional Flux Modulation," *IEEE Transactions on Energy Conversion* 32, no. 2 (2017): 424–435, https://doi.org/10.1109/tec.2017.2649574.

17. X. Zhao, S. Niu, and W. Fu, "Design of a Novel Parallel-Hybrid-Excited Dual-PM Machine Based on Armature Harmonics Diversity for Electric Vehicle Propulsion," *IEEE Transactions on Industrial Electronics* 66, no. 6 (2019): 4209–4219, https://doi.org/10.1109/tie.2018.2863211.

18. R. Hosoya, H. Shimada, and S. Shimomura, "Design of a Ferrite Magnet Vernier Machine for an In-Wheel Machine," in *2011 IEEE Energy Conversion Congress and Exposition* (2011), 2790–2797.

19. H. Qu, Z. Q. Zhu, T. Matsuura, et al., "Comparative Study of Dual PM Vernier Machines," *World Electric Vehicle Journal* 12, no. 1 (2021): 12, https://doi.org/10.3390/wevj12010012.

20. S. Jia, P. Sun, S. Feng, P. Chen, D. Liang, and J. Liu, "Analysis and Experiment of a Dual Stator/Rotor PM and Winding Flux Modulated PM Machine," *IEEE Transactions on Industry Applications* 59, no. 2 (2023): 1659–1669, https://doi.org/10.1109/tia.2022.3227887.

21. Y. Gao, T. Kosaka, Y. Liu, M. Doppelbauer, and R. Qu, "Comparative Analysis of Double Flux Modulation Permanent Magnet Machines With Different Stator PM Arrangements," *IEEE Transactions on Industry Applications* 58, no. 2 (2022): 1941–1951, https://doi.org/10.1109/tia.2021.3138838.

22. W. Zhao, Q. Hu, J. Ji, Z. Ling, and Z. Li, "Torque Generation Mechanism of Dual-Permanent-Magnet-Excited Vernier Machine by Air-Gap Field Modulation Theory," *IEEE Transactions on Industrial Electronics* 70, no. 10 (2023): 9799–9810, https://doi.org/10.1109/tie.2022.3217583.

23. S. Niu, T. Sheng, X. Zhao, and X. Zhang, "Operation Principle and Torque Component Quantification of Short-Pitched Flux-Bidirectional-Modulation Machine," *IEEE Access* 7 (2019): 136676–136685, https://doi.org/10.1109/access.2019.2942482.

24. X. Zhao, S. Niu, and W. Fu, "Torque Component Quantification and Design Guideline for Dual Permanent Magnet Vernier Machine," *IEEE Transactions on Magnetics* 55, no. 6 (2019): 1–5, https://doi.org/10.1109/tmag.2019.2894872.

25. H. Xu, Z. Q. Zhu, Y. Zhou, and L. Chen, "Contributions of Stator and Rotor PMs in Dual-PM Machines With Different Stator and Rotor Pole Number Combinations," *IEEE Transactions on Energy Conversion* 39, no. 1 (2024): 516–532, https://doi.org/10.1109/tec.2023.3318122.

26. W. Q. Chu and Z. Q. Zhu, "Average Torque Separation in Permanent Magnet Synchronous Machines Using Frozen Permeability," *IEEE*

Transactions on Magnetics 49, no. 3 (2013): 1202–1210, https://doi.org/10.1109/tmag.2012.2225068.

27. Z. Q. Zhu and W. Q. Chu, "Advanced Frozen Permeability Technique and Applications in Developing High Performance Electrical Machines," *Transactions of China Electrotechnical Society* 31, no. 20 (2016): 13–29.

28. Z. Q. Zhu, "A Simple Method for Measuring Cogging Torque in Permanent Magnet Machines," in *2009 IEEE Power & Energy Society General Meeting* (2009), 1–4.